Military Technical College
Kobry El-Kobbah,
Cairo, Egypt

7th International Conference
on
Chemical & Environmental
Engineering
27 - 29 May, 2014.

CEEC-3

CORROSION PERFORMANCE OF FRICTION STIR WELDED Al-Zn-Mg-Cu ALUMINUM ALLOY TYPE 7010

Mohamed Gobara* and Mahmoud Maher*

Abstract

High strength Al-Zn-Mg-Cu alloy type 7010 has been friction stir welded with a standard M10 threaded tool. Microstructure of the joint was investigated in the transverse welding plan where the typical welding zones are clearly recognized. Corrosion performance along these zones was evaluated using the Open Circuit Potential (OCP) and the Electrochemical Impedance (EIS) techniques in a 3.5% NaCl solution at room temperature. Features of sever corrosion as well as localized pitting were observed in both the Heat Affected Zones (HAZ) and the Thermo-mechanically Affected Zones (TMAZ).

* Egyptian Armed Forces - Military Technical College, Kobry Elkobba, Cairo, Egypt
e-mail m_gobara@yahoo.com

Introduction

The low heat input welding process, namely Friction Stir Welding (FSW), got the motivation to replace the standard fusion welding techniques in massive welding industries such as transportation and shipbuilding. Friction stir welding (was invented by The Welding Institute in England in 1991[1]) overcomes those associate problems arise during solidification and reduces the accompanying Heat Affected Zone (HAZ) around the weld [2]. Generally, the welded joint of aluminum alloys consists of four different microstructural zones namely: the Nugget Zone (NZ), the thermomechanically Affected Zone (TMAZ), the Heat-Affected Zone (HAZ) and the parent Material (PM). The parent material is not affected by the FSW process. Although, the HAZ is affected by heat, it does not show any plastic deformation. In addition, it has the same size and shape of grains of the parent material. TMAZ, close to the nugget, is plastically deformed and heated. The nugget is affected by the highest temperature and the highest plastic deformation during FSW process [3]. The microstructural changes produced during FSW play the main role of changes in both mechanical and corrosion behavior of the welded alloy.

In high strength aluminum alloys, especially the heat treatable type such as 2xxx and 7xxx series, having narrow HAZ with lower residual stresses enhances the mechanical performance of the joint [4-7] Many studies have been investigated the friction stir processing of 7xxx-series aluminum alloy [8-12]. Comprising studies of the recrystallization mechanisms [13, 14] precipitation sequence [15, 16] residual stresses, mechanical properties [17-22] and welding parameters [23].These investigations of the welded joints showed lower yield and ultimate strength compared with the parent material which was attributed to the reduction of the very fine hardening precipitates [16, 24]. However, there are only a few studies related to the corrosion behavior of the FSW aluminum alloys.[23-26] Generally, the welded zones are more sensitive to corrosion than the parent material in heat treated alloys such as AA2024-T3 and AA7075-T6 after FSW processing [3, 27].

In this study, the microstructure of the friction stir welded Al-Zn-Mg-Cu aluminum alloy type 7010 and its impact on the joint corrosion behavior have been investigated. Mutual effect of both the microstructure morphology variation together with the nature of the precipitated (second phase particles MgZn2) have been evaluated using both the Open Circuit Potential (OCP) and the Electrochemical Impedance techniques (EIS).

Experimental Work

The Al-Zn-Mg-Cu alloy type 7010 was supplied by BAE Systems and Airbus UK in the form of rolled plates 6.35mm in thickness and nominal chemical composition (Zn 6%, Mg 2.15%, Cu 1.81%, Zr 0.1%, Fe 0.08%, Mn 0.03%, Cr <0.01%). It was supplied in the over aged state in the temper conditions T7651. Friction stir welding was carried out in the rolling direction using a standard M10 threaded tool on an adapted milling machine. The supplied plates were tightly clamped to a steel table after their edges were mechanically prepared. Welding was performed using a travel speed of 95 mm/min and a spindle speed of 180 r.p.m in the clock wise direction. Hardness profile across the joint different zones (parent material, HAZ, TMAZ and nugget) was measured on the transverse welding plane perpendicular to the weld line, Figureure 1. This profile was measured in positions 1 mm away from both the plate surfaces and in the mid thickness position.

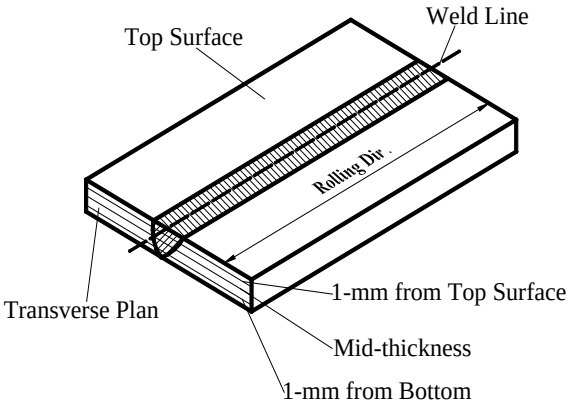

Figureure 1 Schematic drawing showing the measured hardness positions

The hardness measurements were conducted using the Vicker's Armstrong hardness testing machine with 5 Kg load. Optical observation was performed using a Ziess optical microscope equipped with a digital camera connected to a personal computer. To reveal the microstructure, all the observed specimens were exposed to a Keller's reagent for 8-12 sec. Distribution of the minute second phase particles of the etched specimens was examined with the Field Emission Gun (FEG) scanning electron microscope type "Phillips XL30". Chemical composition of these particles was determined by the attached energy dispersive spectroscopy (EDAX). Interaction of these minute grains with both the grains and the sub-grains' boundaries was revealed using the transmission electron microscope at 30 Kv.
The weld corrosion behavior was evaluated using both the Open Circuit Potential and the Electrochemical Impedance spectroscopy techniques. Joints were pre-cleaned using demonized water, rinsed with acetone, air dried at 60ºC for 30 min and finally cooled down to the room temperature. All measurements, in both techniques, were performed using a three-electrode capillary cell where the cleaned joint was used as the working electrode, a platinum wire was used as a counter electrode and finally a standard Ag/AgCl wire was used as a reference electrode. The three electrodes were contained in a Teflon tube with 3mm in inner diameter and 5mm in outer diameter. Measurements were applied, in 6mm step, on the mid-thickness position and on the top surface of the joint. Electrochemical impedance measurements were carried out at the measured Eocp values applying ±10mV perturbation in the frequency range from 1x105 to 10 Hz. All corrosion measurements, for both techniques, were performed separately in 3.5% NaCl solution at room temperature and in open air with a Gamry® reference 600 instruments.

Results and Discussion

Macro and microstructure of the friction stir welded zone through the plate thickness is shown in Figure.2. This microstructure variation in the weld region is developed because of the combined effect of both the material plastic flow and the evolved heat during the stir process. They were proved to be a function of the tool shoulder size, pin geometry, spindle and travel speeds. During stirring, the rolled texture in the parent/supplied material is being broken and the elongated grains are continuously recrystallize to form smaller equaxed structure. In Figure 2a, the macrostructure of the weld shows an onion shape structure which is formed because of the chosen welding parameters. The rolled parent material shows an elongated fibrous structure with an aspect ratio of 0.1 and main length of 100μm as presented in Figure.2b. Symptom of partial recrystallization of these elongated grains is clearly

observed in the interface, thermo-mechanically affected zone (TMAZ), as shown in Figure 2c. Equiaxed recrystallized grains with about 3µm in diameter is shown in Figure 2d. This developed microstructure is a function of the deformation severity that increases as going towards the weld line (centre of the weld).

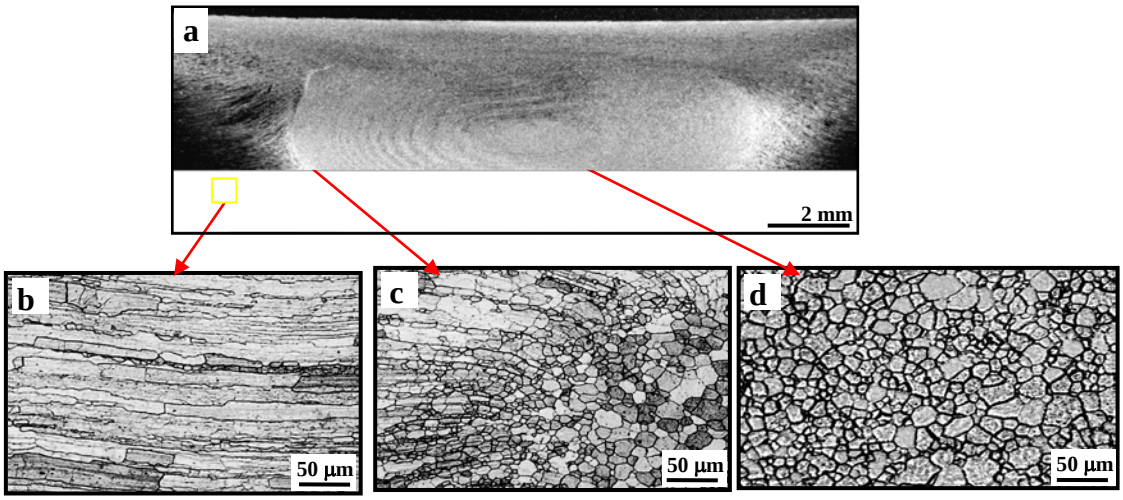

Figure 2 Macro and Microstructure of the FSW at different positions (a) cross section of weld zone, (b) parent material (c) interface zone (d) nugget Zone.

Back scattered electron image of the parent material shown in Figure 3 presents the relatively coarse η precipitates and the constituent particles of Al7Cu2Fe (white areas) on the grain boundaries. Finer dispersoids of ή as well as Al3Zr (black areas) within the parent material grains were investigated using the TEM facility as shown in Figure 4 where they are distributed within the grains as well as their boundaries [14, 15].

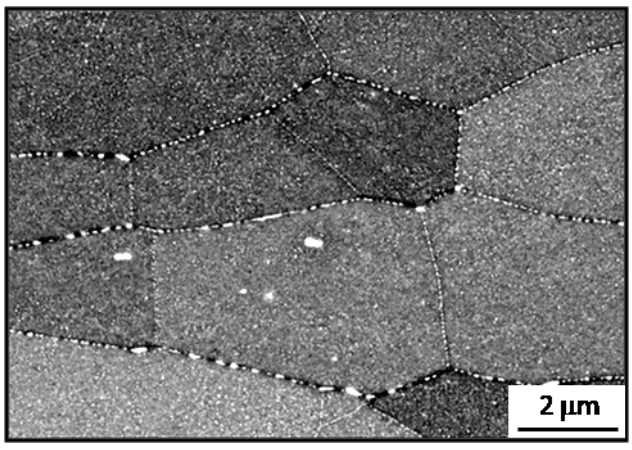

Figure. 3 Relative coarse second phase particles on the grain boundaries of the parent material.

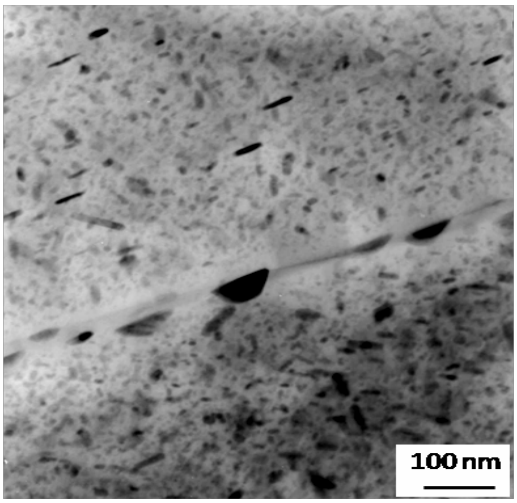

Figure. 4 Fine dispersoids within the grain and its boundaries.

Figure 5 presents the hardness profiles measured through the welding zones in three different positions along the plate thickness as shown in Figure 1. These measured profiles demonstrate a central plateau corresponding to the tool shoulder but with different widths related to bead contour spreading [16, 17]. A maximum value of 150Hv, which is lower than that of the parent material, is measured on the nugget while a minimum value of about 110Hv in the HAZ. As shown in this Figure, the hardness level in the central plateau of the measured three profiles is almost the same even that it was expected to show sensible variation along the weld thickness. This behavior was proved, in other work out of this scope, to take place because of the used high spindle speed over a critical value.

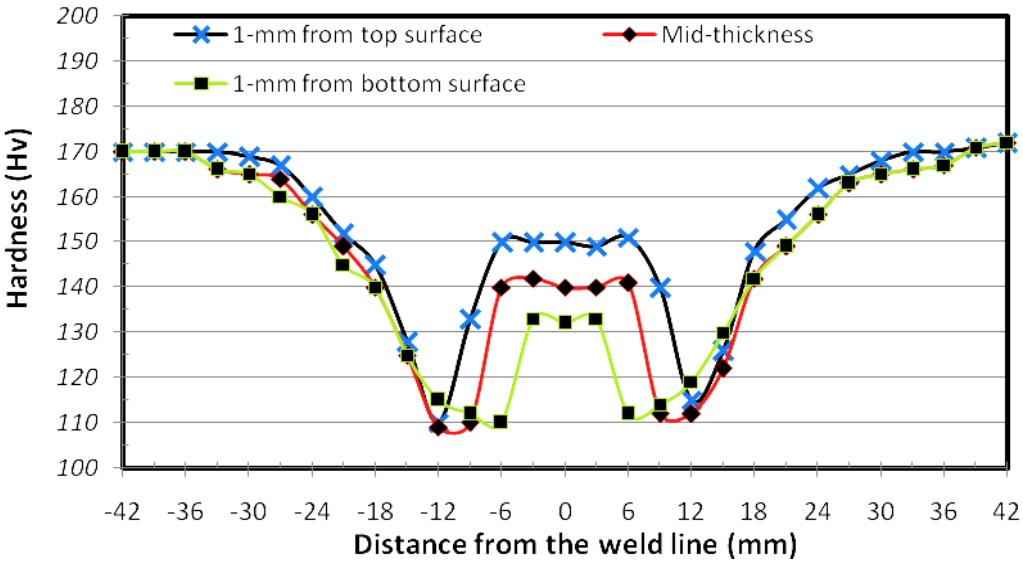

Figure 5 Hardness variation across the weld in three different positions

Figure 6 shows the variation of the open circuit potential measured across the weld, in the mid thickness position of the transverse plane. It shows a mirror profile around the weld line with minimum potential values -812mV in the boundary of the TMAZ and a maximum of -785mV in the parent material. This relatively big difference increases the susceptibility of the

boundary of this zone to chemical corrosion. A slight increase of the measured potential is recorded in the weld core position that may be correlated to the level of residual stresses in the fine equiaxed recrystallized grains as shown in Figure 2d. Typical measurements were performed on the top surface of the weld and shown in Figure 7. The presented profile has almost the same behavior traced in the transverse plane, it shows a minimum and a maximum values in the same order. Although there is a slight difference between the width of the nugget in the mid thickness position and that on the top surface, minimum measured potential is presented in Figure 6 and Figure 7 in the same positions (-12 and 12 mm from the weld centre) because of the available measuring step (6mm a part).

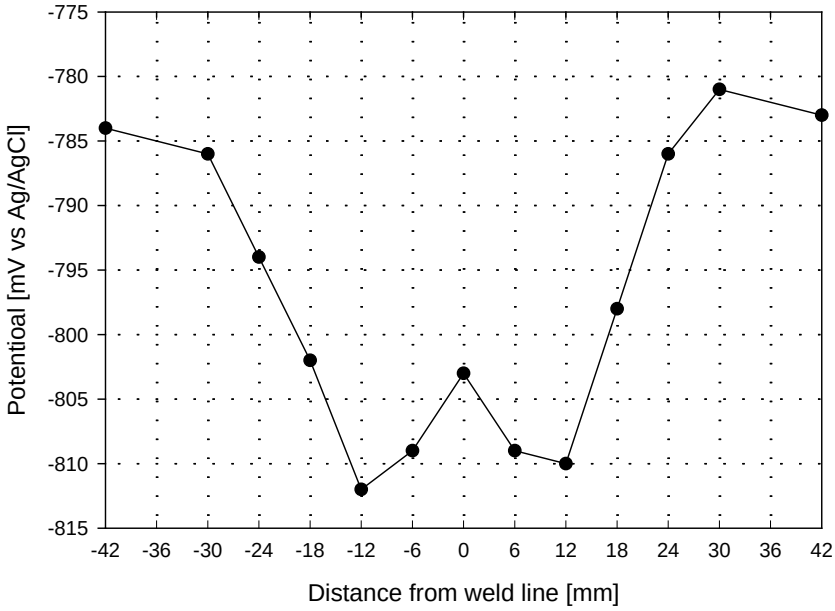

Figure. 6 Potential profile across the transverse plan at the mid-thickness position

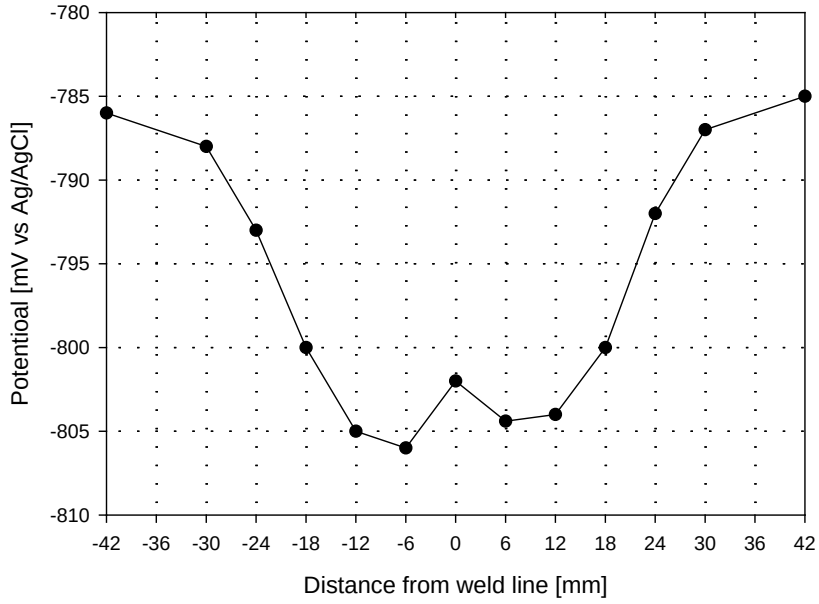

Figure 7 Potential profile across the top surface of the weld

The joint corrosion behavior was also measured with the EIS technique across both sides of the weld in the mid thickness position. For clear presentation, Figure 8 demonstrates the measured values for one side, from the weld line, of the joint with different frequencies. Maximum impedance was measured at the parent material (42 mm from the weld line) whereas minimum value was measured at the TMAZ (12 mm from the weld line).

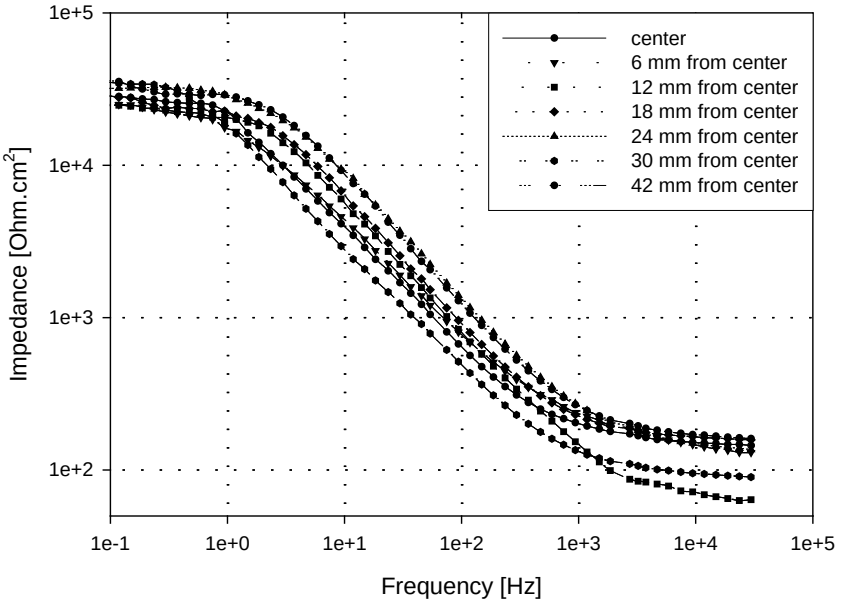

Figure. 8 Impedance behaviour at different points across the weld

For more investigation of the EIS data, the data is fitted to an equivalent circuit shown in Figure 9. The EIS equivalent circuit shown in the Figure 9 is typically for bare samples and is applicable to this welded sample where; R_s represents the solution resistance between the alloy and the counter (platinum) electrode, C the double layer capacitance, R_{ct} is the polarization resistance. A constant phase element, CEP_{dl}, is used in stead of pure capacitance for the double layer. The values of C_{dl} can be calculated for a parallel circuit composed of a *CPE* (Q) and a resistor (R_{ct}). according to the following formula [28]:

$$C_{dl} = \frac{Y_0 \omega^{n-1}}{\sin(n\pi/2)}$$

Where Y_0 is the *CPE* constant, ω is the angular frequency (rad/s), $j^2 = -1$, which is an imaginary number and n is the *CPE* exponent. For ideal electrodes, the *CPE* is equal to an ideal capacitor when n= 1**.**

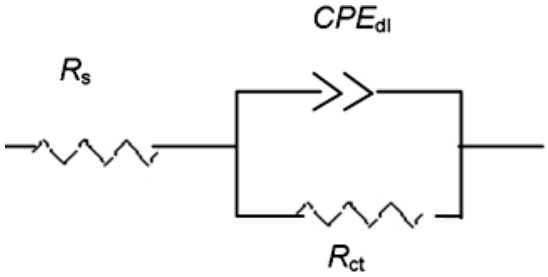

Figure. 9 Equivalent circuits used for numerical fitting of the EIS experimental data

Figure 10 shows the change in charge transfer resistance of welded sample as a function of distance from weld line. From the figure, it can be observed that the R_{ct} values are in consistent with the open circuit potential measurements (Figures 5 and 6), where the maximum resistance is shown at the parent metals (42mm from the weld line) and a minimum resistance is shown at TMAZ (12 mm from the weld line). The R_{ct} values are reflective of processes occurring at the solution/metal interface; i.e. the interaction between the corrosive solution and the metal surface.

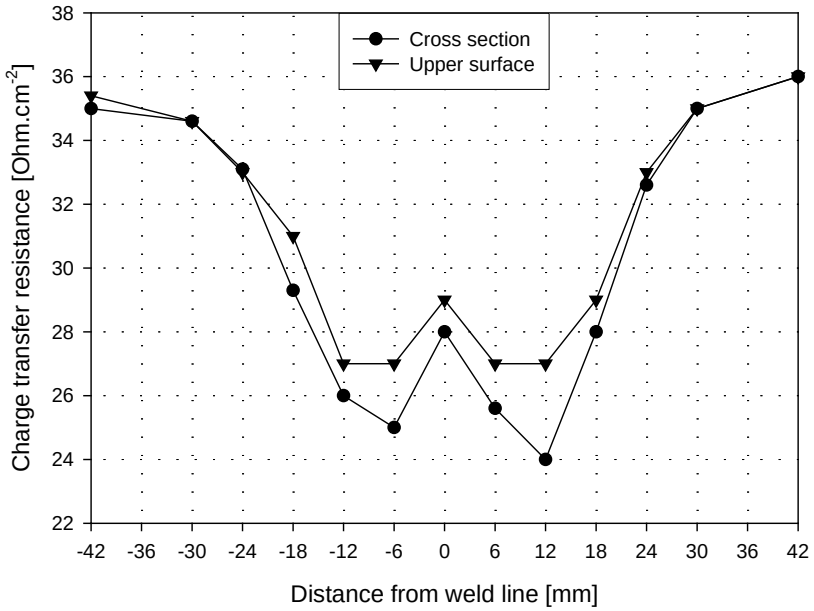

Figure. 10 Charge transfer resistance acoss the weld in 3.5% NaCl solution in the mid-thickness and top surface positions

Visual inspection of the immersed welded joint in the corrosive medium 3.5%NaCl for about 24 hrs notice a develop of a white gelatinous substance covers both the affected zones (TMAZ and HAZ). This gelatinous substance is recognized as $Al(OH)_3$ and always observed on the Al surface as a corrosion product [29]. Prolonged immersing periods (100 hrs) creates corroded regions with different intensities having the pattern shown in Figure11.

Figure. 11 Optical macrograph of the transverse welding plane after 100 hrs immersion in the 3.5% NaCl solution.

Macroscopic observation reveals that one side of the affected zones (Left side) is severely corroded than the other which can be correlated to the residual stress variation in both sides created by the direction of the material flow as well as the inclination angle of the stir tool during the weld process. Variation of this pitting tendency in the observed zones is strongly dependant on the state of microstructure variation as well as the secondary phase

particles distribution. Addition of Zn atoms to the aluminum matrix lowers the alloy potential from -0.85 to -0.96 and -1.03 V SCE as the Zn weight percentage increases from 0%, 2% and 10% respectively [4]. Therefore, the rich Zn second phase particles are associated with relatively negative potentials that enhance the corrosion susceptibility at these regions. As shown in Figures 2 and 3, the rich Zn second phase particles decorate both the grain and sub-grain particles. Relative higher amount of the grain boundaries and consequently the rich Zn particles are observed in the partially recrystallized thermo-mechanically affected regions. Therefore, these affected zones are considered preferable regions for corrosion and localized pitting as shown in Figure 11.

Surface observation with higher magnification (SEM) reveals the difference in the corrosion susceptibility across the joint as shown in Figure 12. Minor corrosion is observed in the parent material (Figure 12-a) as well as the weld nugget, medium corrosion in the heat affected zone (Figure 12-b) and maximum corrosion with localized pitting in the thermo-mechanically affected zone (Figure 12-c). This variation in the corrosion behavior profile is explained as a result of the combined effect of the second phase particles distribution and the accompanied residual stresses in the different weld zones. In the nugget area, the completely recrystallized grains produce large amount of grain boundaries decorated with the second phase particles but with minimum residual stresses. This combination does not enhance the corrosion at this region [30]. In contrary to this state, the partially recrystallized thermo-mechanically affected zone contains comparably large amount of grain boundaries but with higher residual stresses. This combined effect of the remaining residual stresses as well as the large contact area with the Zn containing particles enhances the intergranular corrosion and causes complete grains to be pulled out from their position in the aligned structure as shown in Figure.10b. In the heat affected region, the precipitates are coarsened, loose their coherency and concentrate the corrosion in these localized regions in the form of pitting.

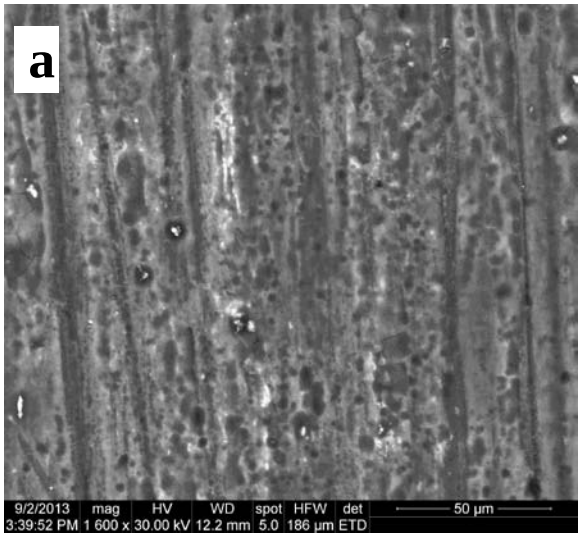

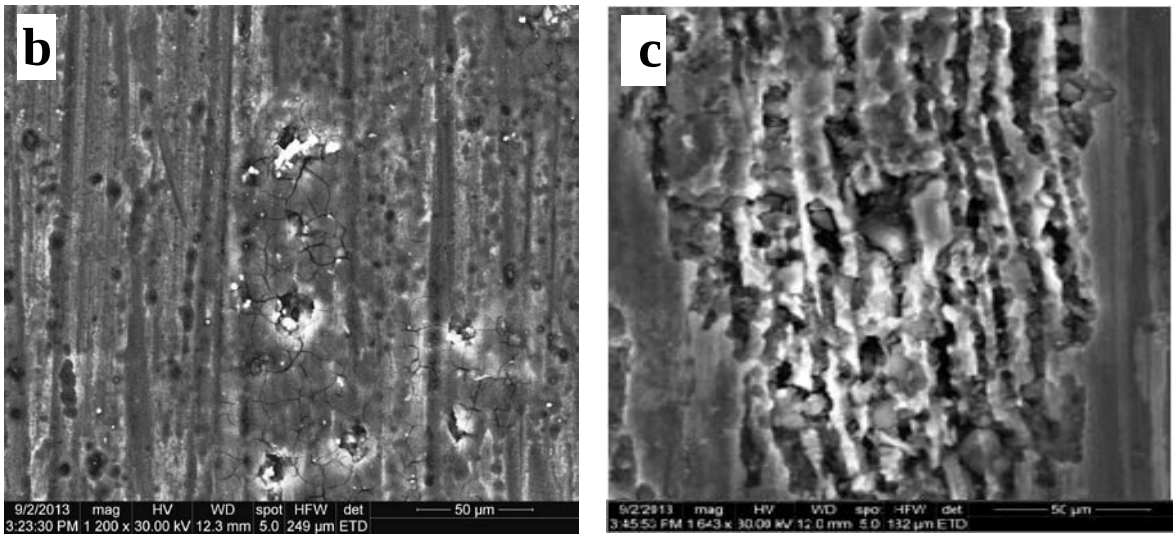

Figure. 12 SEM micrographs showing the corrosion behaviour across the weld in different regions a) parent material b) Heat affected zone c) Thermally affected zone.

Conclusion

1. Corrosion behavior changes across the friction stir joint.
2. Maximum corrosion susceptibility is observed in the heat and thermo-mechanically affected zones.
3. Corrosion performance measured by the open potential circuit technique coincides with that measured by the electrochemical impedance spectroscopy.
4. Corrosion severity depends not only on the existence of second phase particles having lower potentials but also on the accompanied residual stresses.
5. Heat treatment is recommended to reduce the residual stresses in the thermo-mechanically affected zone to normalize its corrosion tendency.

References

1. Thomas, W.M., et al., Friction Stir Butt Welding, U.S. Patent, Editor. 1991, 9125978.8: Great Britain. p. 317.
2. Bahrami, M., et al., Exploring the effects of SiC reinforcement incorporation on mechanical properties of friction stir welded 7075 aluminum alloy: Fatigue life, impact energy, tensile strength. Materials Science and Engineering: A, 2014. 595(0): p. 173-178.
3. Paglia, C., et al. Strength, Corrosion and Environmentally Assisted Cracking of a 7075-T6 Friction Stir Weld. in Materials Science Forum. 2002. Trans Tech Publ.
4. Feng, A., D. Chen, and Z. Ma, Microstructure and cyclic deformation behavior of a friction-stir-welded 7075 Al alloy. Metallurgical and Materials Transactions A, 2010. 41(4): p. 957-971.
5. Fonda, R.W., et al., Microstructure, mechanical properties, and corrosion of friction stir welded Al 5456. Materials Science and Engineering: A, 2009. 519(1–2): p. 1-8.

6. Midling, O.T., L.D. Oosterkamp, and J. Bersaas, Friction stir welding aluminium process and applications. 7th INALCO Conf. Cambridge, UK, 1998.
7. Backlund, J., A. Norlin, and A. Andersson. Friction stir welding-weld properties and manufacturing techniques. in Joints in Aluminium-Inalco, 1998: 7th International Conference. 1999. Woodhead Publishing.
8. Gallais, C., et al., Multiscale analysis of the strength and ductility of AA 6056 aluminum friction stir welds. Metallurgical and Materials Transactions A, 2007. 38(5): p. 964-981.
9. Mishra, R.S. and Z. Ma, Friction stir welding and processing. Materials Science and Engineering: R: Reports, 2005. 50(1): p. 1-78.
10. Svensson, L.-E., et al., Microstructure and mechanical properties of friction stir welded aluminium alloys with special reference to AA 5083 and AA 6082. Science and technology of welding and joining, 2000. 5(5): p. 285-296.
11. Dracup, B.J. and W.J. Arbegast, Friction stir welding as a rivet replacement technology. Training, 1999. 2013: p. 11-25.
12. Mochizuki, M., et al., Fracture toughness of structural aluminium alloy thick plate joints by friction stir welding. Science and Technology of Welding & Joining, 2006. 11(3): p. 366-370.
13. Buffa, G., L. Fratini, and R. Shivpuri, CDRX modelling in friction stir welding of AA7075-T6 aluminum alloy: Analytical approaches. Journal of materials processing technology, 2007. 191(1): p. 356-359.
14. Su, J.-Q., T.W. Nelson, and C.J. Sterling, Microstructure evolution during FSW/FSP of high strength aluminum alloys. Materials Science and Engineering: A, 2005. 405(1): p. 277-286.
15. Sullivan, A. and J. Robson, Microstructural properties of friction stir welded and post-weld heat-treated 7449 aluminium alloy thick plate. Materials Science and Engineering: A, 2008. 478(1): p. 351-360.
16. Rhodes, C.G., et al., Effects of friction stir welding on microstructure of 7075 aluminum. Scripta Materialia, 1997. 36(1): p. 69-75.
17. Shen, Z., et al., Microstructure and failure mechanisms of refill friction stir spot welded 7075-T6 aluminum alloy joints. Materials & Design, 2013. 44(0): p. 476-486.
18. De, P.S., R.S. Mishra, and C. Smith, Effect of microstructure on fatigue life and fracture morphology in an aluminum alloy. Scripta Materialia, 2009. 60(7): p. 500-503.
19. Linton, V.M. and M. Ripley, Influence of time on residual stresses in friction stir welds in agehardenable 7xxx aluminium alloys. Acta Materialia, 2008. 56(16): p. 4319-4327.
20. Hatamleh, O., I.V. Rivero, and A. Maredia, Residual stresses in friction-stir-welded 2195 and 7075 aluminum alloys. Metallurgical and Materials Transactions A, 2008. 39(12): p. 2867-2874.
21. James, M., et al., Synchrotron diffraction measurement of residual stresses in friction stir welded 5383 ‑ H321 aluminium butt joints and their modification by fatigue cycling. Fatigue & Fracture of Engineering Materials & Structures, 2004. 27(3): p. 187-202.

22. James, M.N., D.G. Hattingh, and G.R. Bradley, Weld tool travel speed effects on fatigue life of friction stir welds in 5083 aluminium. International Journal of Fatigue, 2003. 25(12): p. 1389-1398.
23. Gupta, R.K., H. Das, and T.K. Pal, Influence of Processing Parameters on Induced Energy, Mechanical and Corrosion Properties of FSW Butt Joint of 7475 AA. Journal of materials engineering and performance, 2012. 21(8): p. 1645-1654.
24. Xu, W. and J. Liu, Microstructure and pitting corrosion of friction stir welded joints in 2219-O aluminum alloy thick plate. Corrosion Science, 2009. 51(11): p. 2743-2751.
25. Kang, J., et al., In-situ investigation on the pitting corrosion behavior of friction stir welded joint of AA2024-T3 aluminium alloy. Corrosion Science, 2010. 52(2): p. 620-626.
26. Hatamleh, O., P.M. Singh, and H. Garmestani, Corrosion susceptibility of peened friction stir welded 7075 aluminum alloy joints. Corrosion Science, 2009. 51(1): p. 135-143.
27. R.G. Buchheit and C.S. Paglia. Localized corrosion and stress corrosion cracking of friction stir welded 7075 and 7050. in Electrochemical Society, Corrosion and Protection of Light Metal Alloys 2003.
28. Amin, M.A. and M.M. Ibrahim, Corrosion and corrosion control of mild steel in concentrated H2SO4 solutions by a newly synthesized glycine derivative. Corrosion Science, 2011. 53(3): p. 873-885.
29. C. Vargel, M. Jacques, and D. Schmidt, Corrosion of Aluminium. 2004, Amsterdam: Elsevier. 81-109.
30. Wadeson, D.A., et al., Corrosion behaviour of friction stir welded AA7108 T79 aluminium alloy. Corrosion Science, 2006. 48(4): p. 887-897.